Climate Dynamics manuscript No.
(will be inserted by the editor)

The representation of tropical upper tropospheric water in EC Earth V2

M.S. Johnston · P. Eriksson · S. Eliasson · C.G. Jones · R.M. Forbes · D.P. Murtagh

Received: date / Accepted: date

Abstract Tropical upper tropospheric humidity, clouds, and ice water content, as well as outgoing longwave radiation (OLR), are evaluated in the climate model EC Earth with the aid of satellite retrievals. The Atmospheric Infrared Sounder and Microwave Limb Sounder together provide good coverage of relative humidity. EC Earth's relative humidity is in fair agreement with these observations. CloudSat and CALIPSO data are combined to provide cloud fractions estimates throughout the altitude region considered (500 to 100 hPa). EC Earth is found to overestimate the degree of cloud cover above 200 hPa and underestimate it below. Precipitating and non-precipitating EC Earth ice definitions are combined to form a complete ice water content. EC Earth's ice water content is below the uncertainty range of CloudSat above 250 hPa, but can be twice as high as CloudSat's estimate in the melting layer. CERES data show that the model underestimates the impact of clouds on OLR, on average with about 9 $\mathrm{W\,m^{-2}}$. Regionally, EC Earth's outgoing longwave radiation can be $\sim$20 $\mathrm{W\,m^{-2}}$ higher than the observation. A comparison to ERA-Interim provides further perspectives on the model's performance. Limitations of the satellite observations are emphasised and their uncertainties are, throughout, considered in the analysis. Evaluating multiple model variables in parallel is a more ambitious approach than is customary.

Keywords Humidity · Clouds · IWC · Tropics · Climate · Satellite

M.S. Johnston · P. Eriksson · D.P. Murtagh
Department of Earth and Space Sciences
Chalmers University of Technology
SE-412 96 Gothenburg, Sweden
E-mail: marston@chalmers.se

M.S. Johnston · C.G. Jones
Swedish Meteorological and Hydrological Institute (SMHI)
Folkborgsvägen 1, SE- 601 76 Norrköping, Sweden
E-mail: colin.jones@smhi.se

S. Eliasson
Department of Computer Science, Electrical and Space Engineering
Luleå University of Technology,
Space Campus 1, SE-98128 Kiruna, Sweden
E-mail: s.eliasson@ltu.se

R.M. Forbes
ECMWF
Shinfield Park, Reading, Berkshire, RG2 9AX, U.K.
E-mail: Richard.Forbes@ecmwf.int

1 Introduction

EC Earth is currently a global climate model (GCM) that will soon become an Earth system model (ESM). It is developed by several national weather centres and research institutes across Europe (Hazeleger et al, 2010, 2011) and is a model built according to the "seamless prediction" strategy (Palmer et al, 2009). As such, EC Earth uses the European Centre for Medium-Range Weather Forecasts Integrated Forecast System (ECMWF IFS). IFS, which includes a land and ocean component, is a well-studied and proven Numerical Weather Prediction model that is also used in seasonal predictions at ECMWF. This seasonal prediction version of IFS provides the basis for EC Earth but has been modified by the EC Earth developers.

The primary purpose of this study is to contribute to the assessment of EC Earth by evaluating the model with respect to tropical upper tropospheric water (TUTW). This concept encompasses several model variables, where relative humidity (RH), the layered cloud fraction, total high cloud cover, and ice water content are assessed between 500 and 100 hPa. To put the model deficits in a climate perspective, the top of the atmosphere thermal radiation, commonly known as outgoing longwave radiation (OLR which, henceforth, is understood to mean outgoing longwave radiation under "all-sky" conditions), is also added to the list of variables. The representativeness of these variables in EC Earth is investigated by comparison with satellite retrievals. Average and seasonal values, as well as the day-night variations, are considered.

The opportunity to evaluate models for TUTW has never been better. The satellites of the Earth Observation System, that form the so-called A-Train, are providing new and improved information about the upper troposphere. Humidity inside the troposphere is measured by the Atmospheric Infrared Sounder (AIRS, Gettelman et al, 2006) and the Microwave Limb Sounder (MLS, Read et al, 2007). CloudSat provides cloud-penetrating reflectivity values that allow for the study of the spatial distribution of clouds and cloud properties such as ice water content (Stephens et al, 2002). Cloud-Aerosol Lidar and Infrared Pathfinder Satellite Observation (CALIPSO) offers a new possibility of monitoring optically thin clouds (Winker et al, 2007). CloudSat and CALIPSO, together, provide new opportunities to do more in-depth studies of cirrus clouds and provide datasets that allow for detailed comparisons with climate models (Chepfer et al, 2008, 2010). This is important as older datasets that concern clouds and cloud properties, such as the International Satellite Cloud Climatology Project (ISCCP, Rossow and Schiffer, 1991), have been shown to underestimate the high cloud coverage (e.g., Evan et al, 2007). These problems originate in the inade-

quate spatial resolution and cloud penetrating capabilities of traditional passive optical and infrared sensors. Finally, the Cloud and Earth's Radiant Energy System (CERES) sensors provide a dataset that can be seen as the standard today for the Earth's radiation budget.

However, satellite retrievals have limitations and considerable uncertainties, and a secondary aim of the study is to investigate and highlight these aspects. For example, for which conditions is it possible to make a direct comparison between averages of model data and satellite retrievals? What conclusions can be drawn when model and satellite data differ in respect to definition or sampling of the atmosphere? A general consideration in this context is the cloud penetration capability. Optical and infrared sensors are highly sensitive to the presence of clouds. The exact impact of this strong cloud scattering depends on the target of the observations, but consistently the atmosphere below high clouds are poorly sampled by such techniques. Microwaves are less sensitive to cloud scattering in general, particularly to small ice particles, and this gives a much more even sampling of the atmospheric volume. On the other hand, this means that CloudSat tends to miss high thin clouds, and for MLS, the limb sounding geometry partly removes this advantage.

The structure of the paper is as follows: Sec. 2 discusses the model and the variables evaluated. Sec. 3 introduces the observations used. The direct results are presented and discussed in Sec. 4 and a more overview discussion and a summary are given in Sec. 5.

2 EC Earth

A general overview of the model is given by Hazeleger et al (2011). Technical information about IFS is given in documentation for cycle 31r1 (`http://www.ecmwf.int/research/ifsdocs`). Changes made to IFS during its implementation into EC Earth are listed in the online documentation (`http://ecearth.knmi.nl`). Only an overview of some pertinent information such as configuration, variable description, as well as modifications made to the model, is given in this section. This study uses the atmospheric only configuration of EC Earth, version 2, that is being used in the Atmospheric Model Intercomparison Project (AMIP). AMIP is supported by World Climate Research Programme Working Group on Numerical Experiments and focuses on atmospheric models. AMIP is not meant for climate change prediction.

2.1 Configuration

The standard model configuration uses a spectral resolution of T159 (approximately $1.1^\circ \times 1.1^\circ$) reduced Gaussian grid. The vertical resolution is 62 non-evenly spaced, hybrid levels extending up to about 5 hPa (approximately 37 km). Due to the different horizontal resolutions of the model and satellite datasets, both are re-sampled to a common $5^\circ \times 5^\circ$ resolution. At this resolution, errors due to sampling are reduced (e.g., Eliasson et al, 2011). In addition, since the model output is every third hour, it is necessary to temporally interpolate the data to match the A-Train overpasses.

EC Earth uses prescribed monthly mean boundary conditions, such as sea surface temperature (SST), sea ice, and surface albedo. These are taken from the ERA-Interim dataset (Dee et al, 2011) and are interpolated to give quasi-daily values. The model was run for the period 200612-200711 with a time step of one hour and the model state is saved every third hour. This time period is chosen as it coincides with many of the A-train datasets that starts in 2006. The length of the analyses, one year, is enough to assess such things as representativeness of TUTW (Meehl et al, 2007) and where the model performs poorly. It is, however, not enough to assess climate features such as the El Niño/La Niña-Southern Oscillation sea surface temperature variability.

2.2 Relative humidity

EC Earth bases its RH on the "Teten" saturation vapour pressure parametrization. For more details see the online documentation for IFS cycle 31r1. The RH provided by AIRS and MLS uses, however, the Groff-Gratch expression instead. In the mixed phase, the observations employ a linear treatment of the saturation vapour pressure as a function of temperature (Sec. 3). In the model, a quadratic function is used. The involved expressions for saturation pressure can differ, especially at temperatures below 200 K, by approximately $1-2\%$ (Murphy and Koop, 2005). Therefore, the RH from the model is not used in its original form. Instead, RH is derived from the specific humidity in a similar manner to the satellite data (Gettelman et al, 2006).

Supersaturation with respect to ice is allowed in EC Earth in clear sky (Tompkins et al, 2007). When the supersaturation reaches the ice nucleation limit, which is a function of temperature and can reach 150% (Kärcher and Lohmann, 2002), ice cloud is formed. Once ice is present, the deposition process is considered to be sufficiently rapid relative to the model time step that it can be approximated by a diagnostic adjustment to exactly saturated conditions inside the cloud. In partially cloudy grid boxes, therefore, the cloudy fraction is assumed to be saturated with respect to ice whereas the clear sky fraction is free to be subsaturated or supersaturated.

2.3 Cloud fraction and cirrus cloud cover

The model cloud fraction is the horizontal fraction of a model grid box filled by clouds. In the vertical, clouds are assumed to cover the grid box. A cloud overlap assumption of maximum-random (Geleyn and Hollingsworth, 1979) is assumed for all cloud layers within the column. Cloud layers, with no clear layers in between, are maximally overlapped, whereas cloud layers separated by clear layers are randomly overlapped. The high cloud cover diagnostic is

determined by applying the maximum-random assumption to cloud layers above a pressure level of 45% of the surface pressure. This corresponds to about 440 hPa which follows the ISCCP definition (Sec. 3.5).

2.4 Ice water content

There are three categories of ice water particles in EC Earth, where separation into non-precipitating and precipitating ice is determined by a critical mixing ratio threshold. The first is cloud ice, expressed in units of $\mathrm{mg\,m^{-3}}$, representing smaller ice particles with low sedimentation speed. This category of ice is treated prognostically and is used in the radiation calculations. Precipitating ice represents larger, faster precipitating particles that are generated by either (1) the large-scale cloud microphysics scheme, denoted as LSPI, or (2) the convection scheme, denoted as CPI. Both these latter categories are diagnostic variables calculated as vertical ice fluxes ($\mathrm{kg\,m^{-2}\,s^{-1}}$) in the model and are not seen by the radiation scheme.

The fluxes of ice in EC Earth are parametrized differently for large-scale and convective situations. The CPI flux extracted from the model contains the effects of two different velocities: one for generation of precipitation strong enough to overcome updraught (Liu and Orville, 1969) and another for sublimation (Kessler, 1969). The LSPI flux includes only a velocity for sublimation that is the same as the one used for the CPI flux. No explicit fall velocity is used for melting. Also, the model approximates the sedimentation process for cloud ice using a constant fall speed independent of mass and chosen to avoid numerical discontinuities. The sedimentation rate for cloud ice is modified for temperature and pressure following Heymsfield and Iaquinta (2000) to account for increasing drag on falling ice particles in denser air:

$$v = v_{ref}\left(\frac{p}{p_{ref}}\right)^{-0.178}\left(\frac{T}{T_{ref}}\right)^{-0.394}, \tag{1}$$

where $p_{ref} = 300\,\mathrm{hPa}$, $T_{ref} = 233\,\mathrm{K}$, and $v_{ref} = 15\,\mathrm{cm\,s^{-1}}$.

CloudSat estimates the total ice water content, including precipitating ice. Therefore, a model-retrieval comparison of vertical ice water content profile requires the inclusion of all model ice types. As such, the fluxes are converted to ice water content using an assumed velocity for microphysical conversion rates such as sublimation. The converted fluxes are then added to the cloud ice to as

$$\mathrm{IWC} = \left(\frac{F}{v}\right)_{LSPI} + \left(\frac{F}{v}\right)_{CPI} + CI, \tag{2}$$

where F and v are ice mass flux and fall speed, respectively, CI represents cloud ice, and IWC, the total ice water content. As discussed above, the precipitating ice fluxes in the model fall with different fall speed assumptions and undergo modifications due to phase changes where another fall speed is applied. The speeds are not consistent with each other and so, after the fluxes are extracted, some fall speed assumption must be selected in order to convert them to ice densities. In this study, a mass-independent fall speed following Eq. 1 is used, with v_{ref} set to $1\,\mathrm{m\,s^{-1}}$ for both LSPI and CPI.

For some calculations the quantity ice water path (IWP) is used and defined as

$$\mathrm{IWP} = \int_{z_1}^{z_2} IWC(z)\,dz. \tag{3}$$

2.5 Outgoing longwave radiation

The radiation scheme in EC Earth uses the Rapid Radiation Transfer Model (Mlawer et al, 1997). The scheme requires information about the model's atmospheric state. Variables that affect the radiation calculation include cloud fraction, cloud ice, atmospheric temperature, water vapour, aerosols, greenhouse gases concentration. The model calculates absorption and emissivity over a series of discrete spectral intervals between 10 and $3000\,\mathrm{cm^{-1}}$. First, thermal emittance, or outgoing longwave radiation, with clouds removed is calculated and defined as $\mathrm{OLR_{CS}}$. This is also a pre-step to calculate the actual thermal emittance in the presence of clouds (OLR). Both radiation fields are accumulated in EC Earth and are therefore averaged over the post-processing period (3 hours). The direct effect of aerosols on the climate is taken into account in EC Earth by coupling climatological aerosol concentration fields to the radiation scheme.

The spectral emissivity, and thus longwave radiative properties, are a function of ice water path taken between the cloud base and top. The emissivity is combined with cloud fraction to form an effective cloud fraction to which is added the effect of cloud overlap (Räisänen, 1998). Ice crystal effective radius, in μm, is set as

$$\mathrm{r_e} = 326.3 + T_c(12.42 + T_c(0.197 + T_c 0.0012)), \tag{4}$$

where T_c is the temperature in Celsius. In EC Earth r_e is only allowed to vary between 30 and 60 μm. The longwave optical depth, τ in EC Earth is defined as

$$\tau = 1.66(\alpha + \gamma/r_e)IWP, \tag{5}$$

where α and γ are spectrally dependent coefficients (Ebert and Curry, 1992). Finally, the emissivity is defined as

$$\varepsilon = 1 - exp(-\tau). \tag{6}$$

2.6 Cloud and convection schemes

The fundamentals of the cloud scheme used in EC Earth are described in Tiedtke (1993). The scheme has prognostic variables for grid-box mean humidity, grid-box mean cloud condensate and cloud fraction. Precipitating rain and snow from the large-scale (stratiform) and convective cloud parametrizations are diagnostic. Total cloud cover is derived from the cloud fraction field and the maximum-random overlap assumption in the vertical. The cloud condensate variable is separated into cloud water and cloud ice in the mixed phase (0°C to -23°C) by a quadratic function of temperature.

Clouds are described by their their bulk properties such as volume-averaged cloud water and cloud ice content, as well as by total fractional area (Tiedtke, 1993). Convection provides detrained humidity, cloud condensate (liquid or ice depending on temperature), and cloud fraction at levels determined by the strength of the convection (shallow, mid-level, or deep). In this way, the convective anvils have a radiative impact and the detrained cloud condensate and cloud fraction are treated by the large-scale microphysics scheme. For both large-scale and convection cases, clouds are formed when the grid-box mean RH exceeds a critical threshold of 80%, which implicitly assumes sub-grid variability in the clear-sky humidity field.

3 Observations

The A-Train is a set of sun-synchronous satellites. A unique feature of the A-Train is that all of the satellites observe overlapping areas of the atmosphere, using different techniques, and within a time period of twenty minutes. The ascending node of the satellites is such that they cross the equator around 13.30 (day) and descending around 01:30 (night), local time. In this study, measurements of RH are provided by AIRS and MLS while cloud fraction and high cloud coverage are taken from CloudSat and CALIPSO-based dataset. CloudSat is also the source of ice water content measurements. OLR data are obtained from the CERES centred on the Aqua satellite. High cloud coverage is also taken from the ISCCP D2 dataset. The satellites that make up the ISCCP dataset is not part of the A-train, but constitutes an important link to other satellite datasets.

3.1 Atmospheric infrared sounder

Information about the AIRS sensor and algorithms can be found in, e.g., Gettelman et al (2006). AIRS provides a level 3 RH product derived from the temperature and water vapour. This study uses monthly mean level 3 data from the IR-AMSU version 5 AIRX3STMV5 dataset (Maddy and Barnet, 2008). In this study AIRS data are only used at pressures ≥ 260 hPa (Liang et al, 2011). The horizontal resolution at nadir is approximately 13.5 km. The vertical resolution is highest near the surface at around 2.5 km and decreases with height to around 4 km at 200 hPa. The systematic retrieval uncertainty is assumed to be 15 – 25%, following the AIRS on-line documentation (`http://disc.sci.gsfc.nasa.gov/AIRS/documentation/`).

Specific humidity is converted to RH following the Groff-Gratch formulation for saturation vapour pressure. For temperatures below 253 K, the saturation pressure with respect to ice is applied, while above 273 K the one with respect to water is taken. Between these two temperatures, a transition is obtained by weighting, linearly, the two saturation pressures (Gettelman et al, 2006). Furthermore, AIRS retrieval algorithm only processes scenes where the fractional cloud coverage is no greater than 70% leading to an under-sampling of cloudy scenes.

3.2 Microwave limb sounder

MLS is a limb sounding instrument measuring emission in bands around 118, 190, 240, 640 and 2250 GHz. The sensor is described by Waters et al (2006) and for a description of the RH product see Read et al (2007). MLS measures atmospheric humidity at 190 GHz and temperature at 118 GHz. The conversion from specific to relative humidity is the same as for AIRS. This study uses the daily level 2 product from version 3.3 to create monthly means. The vertical resolution for RH is 4 – 6 km, the along-track resolution is 200 – 300 km and the cross-track resolution is 6 – 12 km. The data were screened following the guidelines in the MLS on-line Data Quality and Description Document (`http://mls.jpl.nasa.gov/data/v3-3_data_quality_document.pdf`). The possible systematic error is said to be 20 to 35%. The MLS retrieval can produce data with high supersaturation. After the standard data screening, all data having a value above 119% were set to this value. This affects about 1.6% of the data globally, but at 200 hPa in the Tropics, this number is higher and varies from season to season. In addition, MLS also undersamples cloudy scenes, especially in regions of deep convection where scattering from cloud ice severely affects the microwave emission (see Liang et al, 2011, Fig. 1 plot d).

3.3 CloudSat

CloudSat is a cloud profiling radar with a horizontal resolution of approximately 2 km. This active sensor operates at 94 GHz and measures the amount of back-scattered signal as a function of distance from the sensor. The vertical profile has 125 bins that are about 240 m thick and each profile is produced every 1.1 km along the orbit. More details are given in Stephens et al (2002).

In this study, ice water content from the Cloud Water Content Radar Only (2B-CWC-RO) dataset is used. This dataset was selected as the retrieval is identical for both day and night conditions. A detailed description of the cloud water retrievals is given in Austin et al (2009).

The 2B-CWC-RO retrievals use only radar reflectivity values. There is no inherent way to determine the water phase of the particles. In a first step, liquid and ice water are retrieved separately. All clouds are treated as if they consist either solely of water or ice particles, independently of temperature. The final ice water content profile is set to zero for temperatures above 0°C, while for temperatures below -20°C the "ice-only" data are taken. Between these temperatures, a linear transition, as a function of temperature, is applied.

The ice water content retrieval assumes a log-normal ice particle size distribution. This assumption constitute the main retrieval uncertainty with an error estimated to 40% (Austin et al, 2009). In addition, errors stemming

from the fact that ice and water particles cannot be discriminated contributes to the uncertainty.

So far, all CloudSat data products are provided on a per profile basis and no cloud fraction estimates are given. Seasonal cloud fraction is here derived by treating all bins with a zero ice water content as cloud-free and non-zero ice water content as cloudy bins. That is to say, the cloud fraction is taken as the fraction of bins with ice water content greater than zero at each level for each geographical area. High cloud coverage is derived in the same manner, but taking into consideration if there is any ice water content greater than zero for pressures below 440 hPa (following the ISCCP definition, Sec. 3.5)

3.4 CALIPSO

The CALIPSO lidar, which operates at wavelengths 532 and 1064 nm, is able to detect very thin clouds with a visible optical depth of 0.01 or less, and can discriminate between spherical and non-spherical cloud particles (Winker et al, 2007). A dataset, called the GCM-oriented CALIPSO cloud product, is specifically designed for the evaluation of clouds in GCMs (Chepfer et al, 2010). This CALIPSO-based dataset is created on geometric height levels from surface up to 19 km but in this study they are converted to pressure levels. This is done using the COSPAR International Reference Atmosphere (CIRA-86) climatology via a simple linear interpolation. The dataset chosen for this study is the $2.5^\circ \times 2.5^\circ$ 3D cloud fraction dataset designed for used with AMIP/CMIP5.

3.5 International Satellite Cloud Climatology Project

The International Satellite Cloud Climatology Project (ISCCP) provides datasets made up of information from geostationary and polar orbiting satellites. The data are based on IR and/or visible (VIS) channels. The dataset covers a long time period and gives information down to 30 km resolution and 3-hour interval (Rossow and Schiffer, 1999). This study uses the D2 dataset that comes on an equal-area grid (Rossow and Garder, 1984), with a horizontal resolution of $2.5^\circ \times 2.5^\circ$.

ISCCP defines high clouds as cloud top pressures less than 440 hPa, from which the definition of high cloud coverage follows. There are several ISCCP retrievals that include data from optical sensors but the IR-only retrieval was selected for this study. This choice provides comparable day and night data but is less sensitive and can underestimate high cloud coverage by $10-20$ pp compared to high cloud coverage from IR+VIS retrieval (Rossow and Garder, 1984). The ISCCP data are interpolated to the match the A-Train passages such that the daily mean becomes an average of these two times.

3.6 Cloud and Earth Radiant Energy System

A detailed description of the CERES sensor is given in Wielicki et al (1996) and its performance is discussed in Loeb et al (2009). This study uses the Single Scanner Footprint top of the atmosphere (TOA)/Surface Fluxes (SSF) and Clouds edition 2.5 (CERES Aqua SSF1deg-lite_Ed2.5) monthly mean dataset, which is centred on the A-Train EOS satellite Aqua (Loeb and Kato, 2002). In short, the SSF dataset consists of monthly means of Earth's thermal emittance under both average "clear-sky" ($\mathrm{OLR_{CS}}$) and cloudy conditions (OLR). These monthly means are obtained by taking the mean of the two daily measurements and assuming that atmospheric conditions in between them remain constant. The uncertainty in the OLR is primarily due to calibration errors (Loeb et al, 2009) and is estimated to be approximately $\pm 5\,\mathrm{W\,m^{-2}}$.

The uncertainty estimation for $\mathrm{OLR_{CS}}$ is more complicated because, in addition to errors in common with OLR, there are remaining cloud effects. Sun et al (2011) estimate that about 50% of the data classified as "clear" in the CERES processing in fact have clouds in the footprint (with optical thickness of <0.3). In addition, CERES "clear-sky" requires a cloud fraction of less than 0.1%. If this criteria is not met during a month, then a default value is used. Also, this implies that the monthly mean $\mathrm{OLR_{CS}}$ in most cloudy regions could consists of just a few measurements. A further complication is that models derive $\mathrm{OLR_{CS}}$ differently; it is calculated over all geographical positions, with clouds removed (Sec. 2.5). This quantity cannot be measured by a satellite, and the CERES $\mathrm{OLR_{CS}}$ can differ locally from model $\mathrm{OLR_{CS}}$ by $> 10\,\mathrm{W\,m^{-2}}$ (Sohn et al, 2010). This error and remaining cloud effects should mainly be of opposite sign and partly cancel each other, but to obtain a relatively conservative estimate the possible systematic error for $\mathrm{OLR_{CS}}$ is set to $\pm 7\,\mathrm{W\,m^{-2}}$.

The effect of clouds on the outgoing longwave radiation is defined as

$$\mathrm{OLR_{CE}} = OLR_{CS} - OLR. \tag{7}$$

Any calibration error should be more or less common between the two quantities, hence, cancel when taking the difference, and CERES uncertainty for $\mathrm{OLR_{CE}}$ is speculatively set to $\pm 5\,\mathrm{W\,m^{-2}}$.

3.7 ERA-Interim

The ERA-Interim global reanalyses dataset, based on the IFS cycle 31r2, is described in detail in Dee et al (2011) and the more technical documents can be found at `http://www.ecmwf.int`. The basic configuration of the dataset is a 0.7° x 0.7° horizontal resolution and 60 vertical levels extending to 0.1 hPa (T255L60). However, the data was interpolated to 1.0° x 1.0°. This study uses the 12 UTC analyses monthly mean of daily means and the 24 hour forecast from that model run. A major difference between Era-Interim IFS version and EC Earth's IFS version is the convection scheme. EC Earth uses modifications to the con-

vection scheme from a later model version (IFS Cycle 32r3) described in Bechtold et al (2008). Documentation on the changes in IFS cycles is found at `http://www.ecmwf.int/products/data/operational_system`.

4 Results

This study concerns the Tropics (30°S – 30°N) where the dominant weather is determined by the Hadley and Walker circulations. Convection plays a vital role in this region and occurs along the Inter-Tropical Convergence Zone (ITCZ) and has a distinct seasonal cycle. Four seasons are examined: DJF, MAM, JJA, and SON (December to February etc.). Specific examples are taken from JJA because this is the season when convection is mostly land-based and covers the important South Asian monsoon and also the season with the largest differences between day and night data. Total tropical averages and sub-regional averages are reported. The sub-regions considered, henceforth referred to as just regions, are illustrated in Fig. 1. These are tropical warm pool (TWP), tropical convective land (TCL), and tropical subsidence water (TSW).

The temporal sampling of the model data are done to be coincident with the passages of the A-train satellites. For simplicity the two samples are denoted as "day" and "night", i.e., data corresponding to the passages around 13.30/01.30 local time. If nothing else is stated, reported values are averages between corresponding day and night data.

4.1 Relative Humidity

4.1.1 Assessment of observations

Fig. 2 depicts the average AIRS and MLS vertical profiles for the TCL and TSW regions. A high number of individual retrievals goes into each profile and the final effect of random errors should be negligible. The assumed systematic retrieval errors, defining the shaded areas in the figures, are discussed in Secs. 3.1 – 3.2.

The AIRS profiles are, throughout this study, smooth and slightly increasing with altitude as expected from a maximum of convection detrainment around 200 hPa and above (Folkins et al, 2002). There is a notable minimum in the profile between 400 and 500 hPa, and although MLS does not extend below 316 hPa, there is a tendency also towards lower values. In the TSW region the two observations remain well within the uncertainty zone of each other. This is not the case in the TCL region where the effect of cloud screening on AIRS retrievals is large.

The average MLS profiles are much less smooth than AIRS, most significantly, there is consistently local minimum in the averaged MLS profiles at the 147 and 261 hPa levels. These "kinks" in the data appear regardless of region or the presence of cloud. This indicates that these features might very well be be retrieval artefacts. MLS has its maximum RH at 200 hPa.

Figure 3 shows the horizontal distribution at two pressure levels for JJA season. There is significant variation of the horizontal distributions between the seasons, but AIRS and MLS give, at their respective levels throughout the Tropics, closely matching geographical patterns, such as the position of regions of convection and subsidence, as well as the gradients in between such areas. The absolute RH levels differ, with the largest discrepancies found where AIRS is most affected by clouds, i.e., in convective regions.

The MLS averages at 200 hPa along the ITCZ show extensive areas of supersaturation, mainly found inside the TWP region. Whether MLS averages reach supersaturation, or not, depends strongly on the data filtering. For example, fewer averages above 100% were reported by Ekström et al (2008) using a somewhat different filtering was applied. AIRS minimum RH can generally be found between 400 hPa and 500 hPa.

For the TCL region (Fig. 2), the observations show mainly higher RH during night. Below 200 hPa, MLS and AIRS are in good agreement, except for the JJA season where MLS shows up to 20 pp (percentage points) higher RH during daytime. The latter could possibly be indicating in-cloud moisture from mid-level convection which would be missed by AIRS. Around 150 hPa, MLS gives consistency a higher day-night difference. Liu and Zipser (2009), using an earlier version of MLS, found up to 20 pp higher RH at night over the TCL region near the tropopause over similar regions. In the TSW region, the day-night difference is basically zero according to AIRS, while MLS gives values up to 5 pp with a sign varying both with season and altitude.

RH differences between the observations are partly due to variations in the respective temperature profiles. In order to quantify this influence, a brief examination was conducted. Where the two sensors overlap, the mean temperature profiles are found to be within 1 K of each other, with MLS normally being the slightly cooler of the two. For the day-night differences, the deviation is even less. In the upper troposphere, a 1 K change in the temperature results in $\sim$10% change in the saturation vapour pressure.

In summary, the AIRS RH profiles remain consistently below MLS in strong convective zones such as TCL and TWP (not shown). However, in the relatively convective-free region, TSW, the two measurements converge. This is mostly due to the effects of clouds on both sensors. In general, the differences between the AIRS and MLS, where they overlap, are 10 – 30 pp for the TCL region. Across the entire tropical region (not shown) this difference reduces to about 5 – 10 pp.

4.1.2 Comparison between model and observations

Referring to Figs. 2 and 3, both with respect to averages and spatial patterns, the agreement of EC Earth with MLS is particularly good around 200 hPa. The MLS averages greater than 100% must be interpreted carefully as they are heavily influenced by how one filters the data. Never-

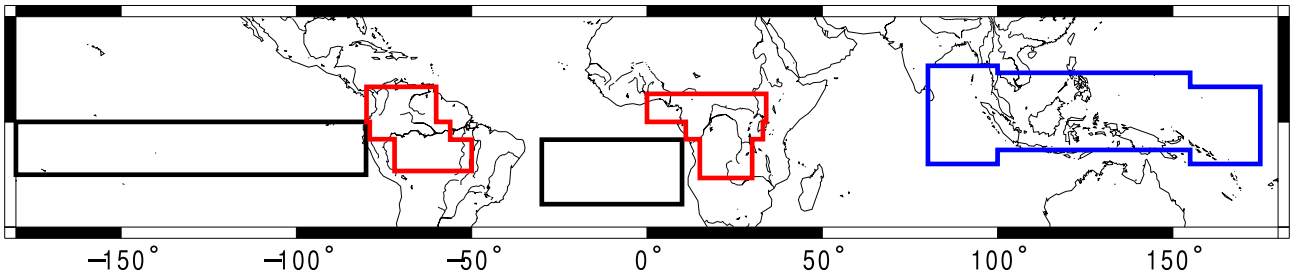

Fig. 1: Selected regions of interest, following Eliasson et al (2011). Black: areas of subsidence denoted as tropical subsidence water (TSW). Blue: Tropical Warm Pool (TWP) consisting of mixed land and water. Red: tropical convective land areas (TCL). Profile values for these regions in subsequent figures are area-weighted means and across multiple regions for TCL and TSW regions.

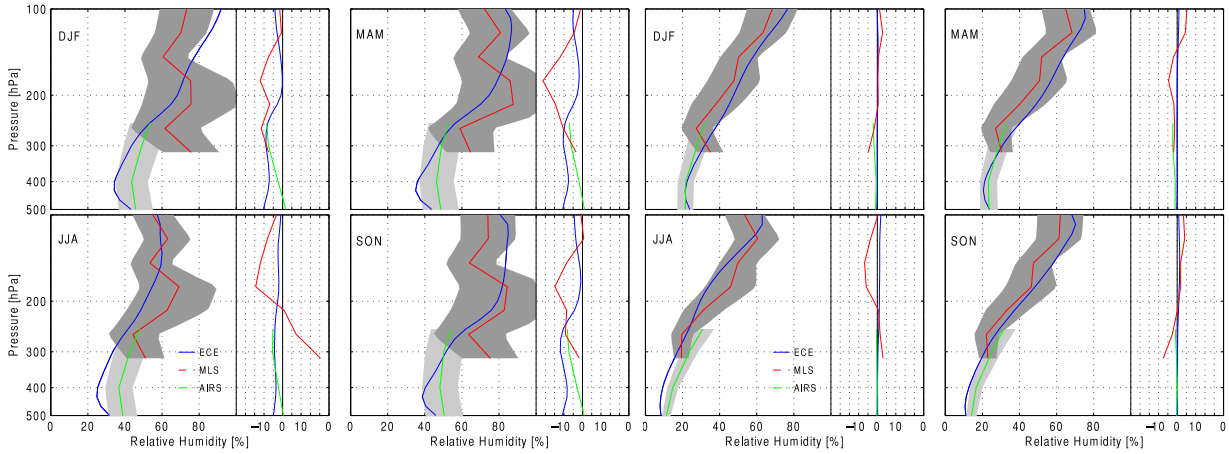

(a) TCL region (b) TSW region

Fig. 2: Seasonal vertical profiles of RH for the TCL and TSW regions. Blue: EC Earth, Red: MLS, and Green: AIRS. The light and dark shaded areas indicate the systematic errors of AIRS and MLS retrievals, respectively (see text for details). In each season and region, the left side shows the mean profiles, while the right side depicts day-night differences in RH (if positive, day value higher).

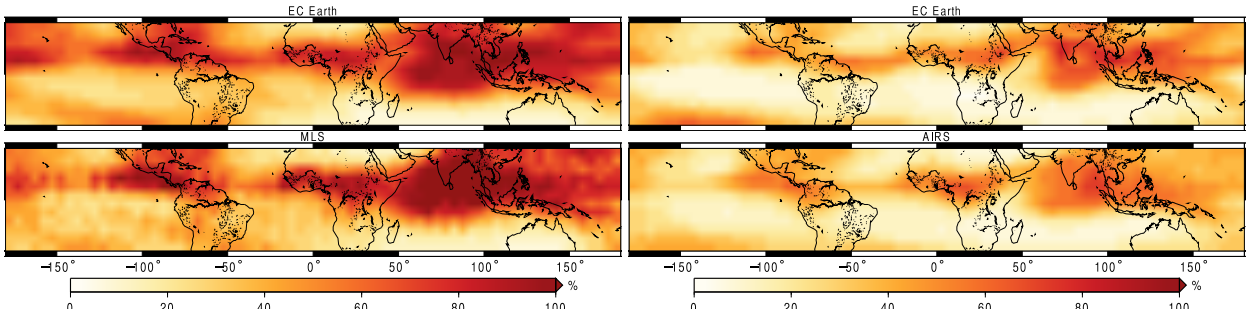

(a) 200 hPa (b) 400 hPa

Fig. 3: Horizontal distribution of RH at 200 and 400 hPa for the JJA. The panels are from top down: EC Earth, AIRS and MLS.

theless, areas with supersaturation seen in the MLS data are also reflected in the model but to a much lesser extent. Areas of MLS supersaturation occur with a frequency of about 2 – 3% with a maximum during JJA. For EC Earth supersaturation is seen only during the JJA season and less than 1% of the time. The salient features of the ITCZ and its branches are consistent between the model and observations. Accordingly, seasonal variability and areas of RH maximum and minimum are also well collocated with regions with frequent clouds and areas of subsidence in EC Earth.

Regionally, the model's mean temperature profiles agree well with AIRS and are within 0.1 K of each other. For MLS, the model tends to be slightly warmer except near 100 hPa. Deviations between MLS and the model are approximately 2 K.

At lower altitudes the agreement between the model's RH and AIRS is poorer. In convective areas, EC Earth is considerably drier, reflecting narrower bands of convection in the ITCZ than is seen in the observations. The ITCZ is best captured for the JJA season, while for other seasons some branches of the ITCZ is not seen at this level in the model but is present in the observation (not shown). This gives considerably stronger vertical gradients in the RH profile for such regions. In the TSW region, the model is slightly drier than AIRS with the exception of the DJF season.

The day-night differences in EC Earth for TCL above 200 hPa show a tendency towards higher RH at night, generally around 2 pp. Similar findings were made by Eriksson et al (2010) for EC Earth, as well as ERA-Interim, and two other GCMs, that concluded that the diurnal cycle of RH in TCL is both underestimated and out of phase compared to observations. Below 200 hPa, there is a much stronger nocturnal signal in the model of up to 10 pp. This agrees with AIRS down to about 350 hPa, but below this level AIRS turns towards a zero difference. For the TSW region, there virtually no change in the EC Earth RH between day and night, consistent with AIRS.

4.2 Cloud fraction

4.2.1 Assessment of observations

There is no single satellite that measures the total layered cloud fraction. So, similar to the previous section, this study uses two satellites to provide a more complete cloud fraction profile in the upper troposphere. CALIPSO's short wavelength makes it sensitive to the sum of geometrical cross-section of particles. This translates to a high sensitivity to small particles. The disadvantage is that the lidar attenuates relatively quickly causing it to miss layers at lower levels. For CloudSat the intensity of the backscatter is rather proportional to the sixth power of the particle diameter. Therefore, clouds consisting of very small particles are often missed but CloudSat is able to penetrate thick clouds. Attenuation of the radar signal is associated only with strong precipitation normally found at altitude below 500 hPa.

Consequently, these sensors detect different, but overlapping, portions of the clouds (see, e.g., Delanoë and Hogan (2010) for examples on parallel observations of the two instruments). For higher altitudes, the CALIPSO cloud product give the highest cloud fraction. At lower altitudes, CloudSat reports higher cloud fraction values, and is a better representation, as the CALIPSO sensor is frequently obscured by cloud layers at higher altitudes. These aspects give also completely different patterns for day-night cloud fraction differences.

The layered cloud fraction vertical profile is illustrated in Fig. 4 while horizontal cloud fraction distributions are shown in Fig. 5. The cloud fraction profiles of CloudSat and CALIPSO intersect, in general, around 200 hPa. The two instruments give also similar cloud fraction spatial patterns along the ITCZ and the TWP region, for 200 hPa, though outside these regions, the CALIPSO gives a higher cloud fraction. For altitudes lower than 250 hPa, CloudSat consistently reports higher cloud fraction. The difference between the observations is often greatest above 200 hPa, sometimes by 10 pp or more. Below, differences can range from a few percentage points in TSW region to 10 pp in other regions. The maximum cloud fraction is consistently found between 200 and 150 hPa which in turn has its maximum ($\sim$50%) over the TWP region (not shown) during the JJA season.

Both the CALIPSO and CloudSat cloud fraction are derived in a conservative manner: avoiding false cloud detections due to noise. That this has been achieved in practice is confirmed by the fact that large areas in, e.g., Fig. 5 are classified as basically cloud free for both sensors as well as agreeing with climatology. For this reason, no uncertainty is assigned to the cloud fraction profiles.

The shaded area in Fig. 4 is instead an indication of the possible range of a cloud fraction defined following the detection threshold of CALIPSO dataset. The lower limit at each altitude is set by taking the maximum value between the two sensors, while the upper limit is the sum of the two individual cloud fraction estimates. The true cloud fraction should be above the lower limits, but could also be above the upper limits. If the latter is the case then the missing cloud fraction comes from clouds at lower altitudes that are below the detection limit of CloudSat and obscured for CALIPSO by higher cloud layers.

The CALIPSO sensor is known to be more sensitive to clouds at night but this has been compensated for in the dataset used to the point where any remaining bias is considered negligible for comparison with GCMs (Nazaryan et al, 2008; Chepfer et al, 2010). Over the TCL region, both sensors report higher cloud fraction (2 – 5 pp) at night below 200 hPa. Above this level CloudSat hints at a higher cloud fraction during the day or no difference at all.

Fig. 6 shows the distribution of high cloud coverage for JJA where the A-Train data have been processed to match ISCCP's definition. ISCCP shows throughout lower values than the other two observation datasets. The low bias compared to CloudSat is consistent with earlier reports on that the ISCCP dataset underestimates high cloud coverage (e.g., Eliasson et al, 2011). The high cloud coverage mean for the Tropics for JJA is around 35% for CALIPSO dataset, 22% for CloudSat, and 13% for ISCCP.

4.2.2 Comparison between model and observations

The assessment of clouds between observations and models must begin with the problem of when do both define a cloud. In the model the effect of clouds on longwave radiation is basically determined by the cloud ice (Eq. 3 and 5). The model grid boxes between 200 and 150 hPa were examined for the smallest cloud ice occurring with a significant frequency. This cloud ice value was multiplied with a typical layer thickness at the same altitude range, and minimum cloud ice water path of around 0.1 g m^{-2} was ob-

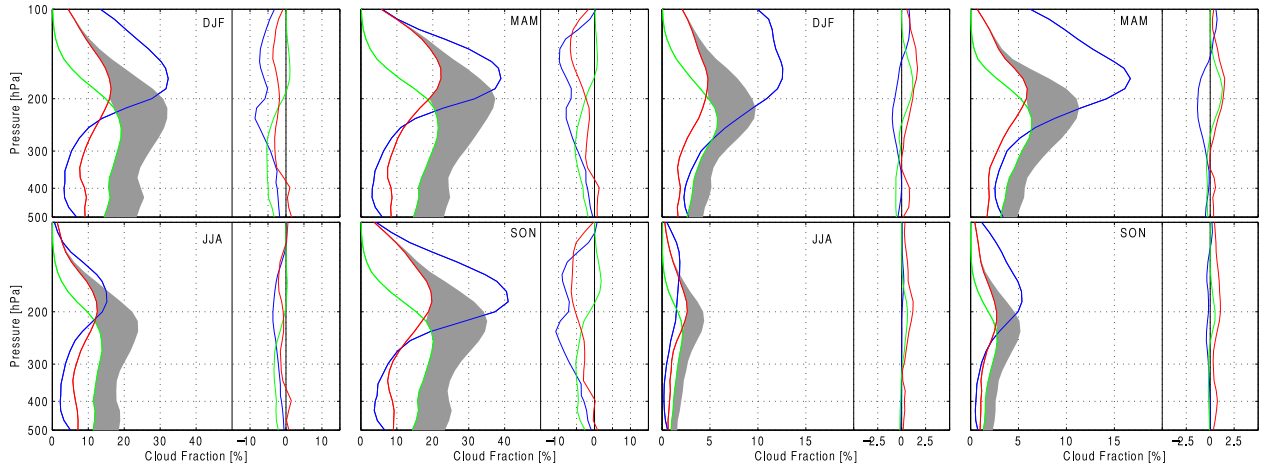

(a) TCL region (b) TSW region

Fig. 4: Seasonal cloud fraction profiles for TCL and TSW regions defined in Fig. 1. Blue: EC Earth, red: CALIPSO cloud product, and green: CloudSat. For each season and region, the plots on the left depicts mean profiles, while on the right are the day-night differences in cloud fraction (if positive, day value higher). Shaded area: a representation of the uncertainty in the observations. See text for details.

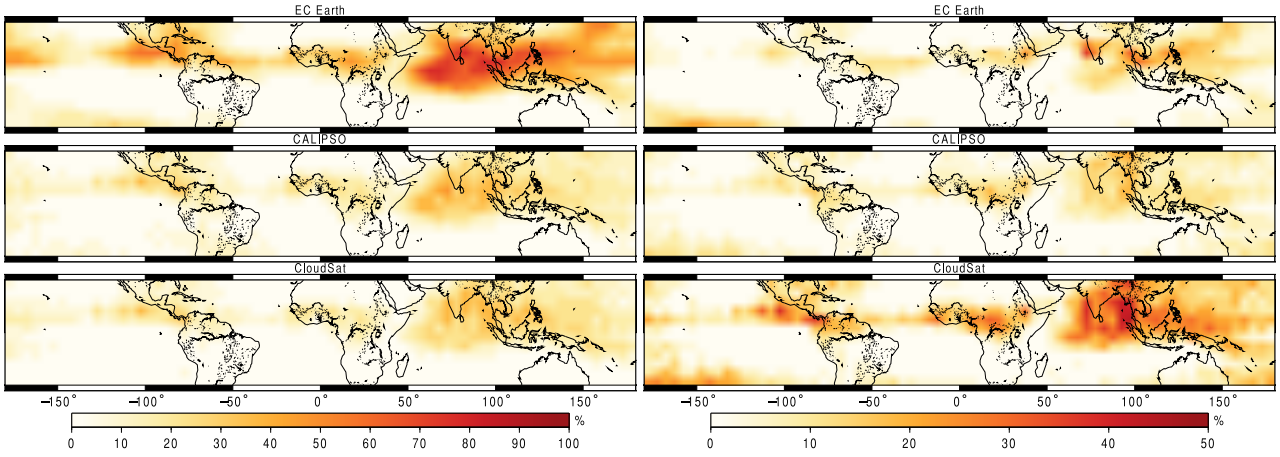

(a) 200 hPa (b) 400 hPa

Fig. 5: Cloud fraction at 200 and 400 hPa for the JJA season. Top panel: EC Earth, middle: CALIPSO, and bottom: CloudSat.

tained. This value was converted to a visible optical depth, τ_v, following Heymsfield et al (2003):

$$\tau_v = 0.065(IWP)^{0.84}, \quad (8)$$

giving a threshold of about $\tau_v = 0.01$. The corresponding value for the CALIPSO dataset is 0.03 – 0.05 (Chepfer et al, 2010). Sub-visible clouds are normally defined as having a VOD of less than 0.03 (Wang et al, 1996). That is, EC Earth includes, to some extent, clouds that are not covered by CALIPSO and can be classified as sub-visible. However, this exercise showed also that the fraction of such sub-visual clouds in EC Earth is marginal (the relative fraction of corresponding cloud ice values is low).

The EC Earth cloud fraction shows different characteristics above and below ∼200 hPa (Fig. 4). Above this level and for all seasons, besides JJA, EC Earth's cloud fraction is above the combined CloudSat and CALIPSO estimates. In fact it is quite often twice the cloud fraction reported by the CALIPSO dataset. The only case of underestimation is JJA in the TSW region, but only up to about 150 hPa. The higher cloud fraction in EC Earth noted here is not explained by the difference in detection threshold compared to CALIPSO dataset, and the conclusion is that EC Earth is too "cloudy" above 200 hPa.

Below 200 hPa, the tendency is opposite. CloudSat's cloud fraction is derived by assuming that any pixel with ice water content above zeros is considered cloudy, which means a cloud fraction that includes precipitation. Assuming that precipitation corresponds to radar reflectivities above 0 dBz, this gives a cloud fraction overestimation of ∼5 pp according to Liu et al (2008, Fig. 4). On the other hand, the CloudSat data used are truncated at $\sim 1\,\mathrm{mg\,m^{-3}}$, even though the actual sensitivity is better (Protat et al, 2010), which results in a decrease of the cloud fraction reported here. Anyhow, the difference between EC Earth and CloudSat below 250 hPa can be at least partly explained

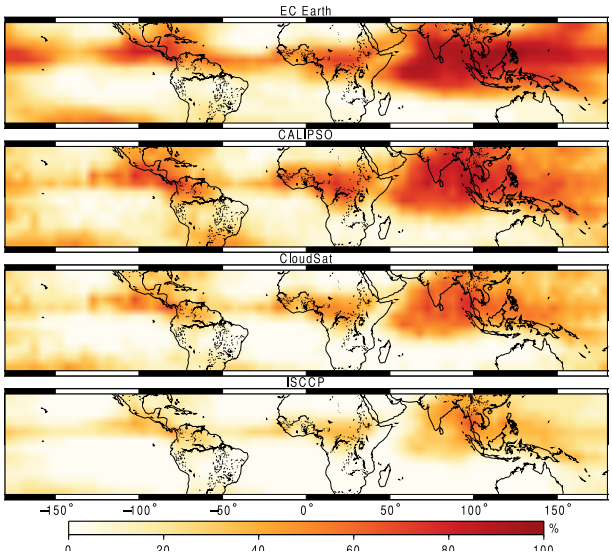

Fig. 6: High cloud coverage for JJA season. Top-down: EC Earth, CALIPSO, CloudSat, and ISCCP.

by the fact that precipitation is not included in the EC Earth cloud fraction, but is present in the CloudSat estimate. Also, the EC Earth cloud fraction here can even be below the CALIPSO cloud fraction. That is, the EC Earth cloud fraction is too low in the lower part of the altitude region considered.

The TCL region in Fig. 4 shows predominantly more clouds at night. While observations and the model all agree below 200 hPa, above this level CloudSat reverses the sign. This deviation between CALIPSO and CloudSat cloud fraction can be understood by considering the different sensitivity of the instruments, in combination with studies such as Soden (2000); Yang and Slingo (2001); Tian et al (2004), showing that the evolution of anvil clouds lag the peak of the convection by several hours. The convection in the TCL areas peaks during the afternoon (Eriksson et al, 2010). In the TSW region, Fig. 4, all differences are less than 2 pp.

4.3 Ice water content

4.3.1 Assessment of observations

Seasonal mean vertical distributions of ice water content for regions TCL and TSW are shown in Fig. 7. For this variable no second data source is included. Comparisons to the only other satellites reporting ice water content are found in Wu et al (2009, MLS) and Eriksson et al (2008, Odin-SMR). However, ice water content from Odin-SMR and MLS cover only the upper troposphere (above 200 hPa) which means they have limited overlap with CloudSat. Protat et al (2010) compared CloudSat 2B-CWC-RO ice water content retrievals with ground-based radar-lidar retrievals over Darwin Australia from 2006-2009. Their results show that CloudSat produces ice water content in too narrow a range and tends to overestimate ice water content below 10 – 11 km by a factor of 2, but is in good agreement above 11 km. CloudSat's sensitivity to precipitation has been established in previous studies such as Waliser et al (2009).

The shape of the CloudSat mean profiles is fairly consistent over the TCL and TWP (not shown) regions. The mean ice water content at 200 hPa for all regions ranges from 2 over the TSW region to 16 mg m^{-3} over the TWP region. The largest ice water content occur over the TWP region with a maximum mean in the vertical of $\sim$30 mg m^{-3}. The point of maximum ice water content is generally found at $\sim$400 hPa with a clear fall off in ice water content below regardless of region.

Figure 8 illustrates the JJA mean horizontal distribution of CloudSat's ice water content (bottom panels) for the Tropics. At 200 hPa CloudSat reports multiple areas of high ice water content ($\sim$40 mg m^{-3}) that are both over land and water. The distribution follows the pattern of the ITCZ and is most extensive in the west Pacific and across southeast Asia. Going from 200 hPa to 400 hPa there is a clear increase in ice water content. This is most striking for the southern part of the Tropics and could be an indication of mid-level convection outside the ITCZ.

The day-night difference (Fig. 7) shows a higher daytime ice water content ($\sim$5 mg m^{-3}), in the TCL region, above 300 hPa but below this is reversed. Over the TWP region (not shown) there is clearly higher nocturnal ice water content of similar magnitude with a peak between 200 and 300 hPa.

4.3.2 Comparison between model and observations

Since CloudSat is most sensitive to the largest ice particles, adding the model's precipitating ice is vital for a representative comparison. This negates the need to try and separate CloudSat ice water content in a similar manner. The representation of the model ice is shown in Fig. 9 with regards to its horizontal distribution. As before, this is examined at 200 and 400 hPa during JJA. The highest concentrations, at both levels, are seen in the western Pacific, Indonesia, and around the Indian subcontinent. These areas of high values are co-located with the ITCZ. At 200 hPa LSPI is nearly absent and cloud ice is clearly the largest component and the most widespread. There is also a notable cloud ice concentration in the TWP region. At 400 hPa there is a clear increase in CPI from 200 hPa and highly concentrated in convective cores along the ITCZ. LSPI shows a 8 fold increase in the TWP but only a 3 fold increase along the ITCZ. Cloud ice, however, shows only a marginal increase.

Vertical ice water content profiles are given in Fig. 7. The mean profiles of cloud ice and LSPI are significantly lower than CloudSat's ice water content. The CPI profiles generally increase sharply below 300 hPa. EC Earth consistently has its maximum ice water content below 500 hPa while CloudSat places its area of highest ice water content above that.

Figure 8 illustrates the horizontal distribution of ice water content in the model. As mentioned in the above paragraph, the cloud ice dominates the model ice at 200 hPa

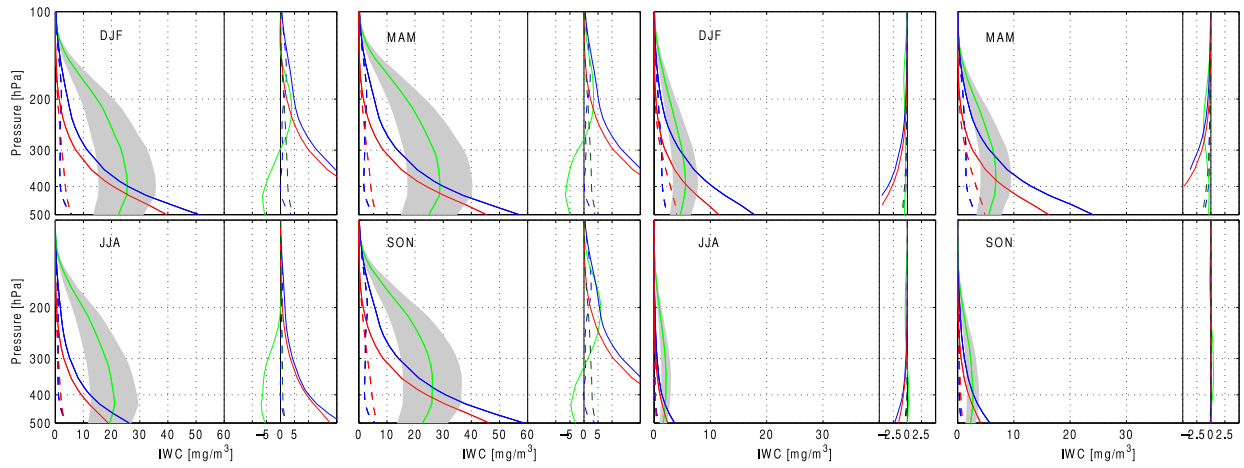

(a) TCL region (b) TSW region

Fig. 7: Ice water content vertical profile for TCL region during JJA. Green: CloudSat, blue (solid): EC Earth ice water content, blue (dashed) EC Earth cloud ice. Red (dashed): LSPI, red (solid) CPI. On the left are the mean profiles and on the right day-night difference. The shaded area is the CloudSat uncertainty of 40%.

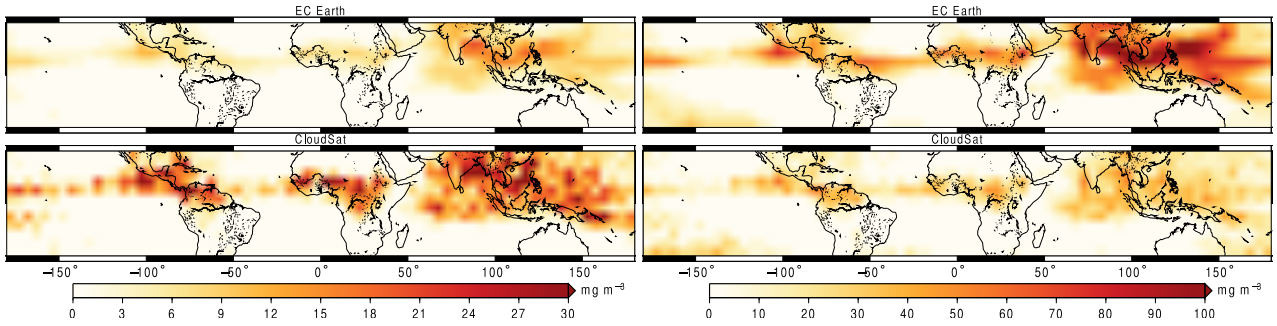

(a) 200 hPa (b) 400 hPa

Fig. 8: Horizontal distribution of ice water content at 200 hPa and 400 hPa for JJA. Top panel: EC Earth ice water content. Bottom panel: CloudSat ice water content.

(Fig. 9), so adding the precipitating ice results in a moderate increase, from 30 to 40% of CloudSat mean ice water content. A significant difference at this level is the occurrence of numerous areas of high ice water content in CloudSat distributed along the ITCZ. This is not seen in EC Earth. At 400 hPa the ice water content in the model is significantly greater than CloudSat but agrees more with regards to the distribution of high ice water content values long the ITCZ.

From Fig. 9, it is clear that it is CPI that is the largest component in the ice water content in EC Earth below 200 hPa. A combination of LSPI and cloud ice, or cloud ice alone, results in poorer ice water content distribution along the ITCZ compared to CloudSat in Fig. 8. Between 200 and 400 hPa cloud ice amounts to about 10 – 30% of the total ice reported by CloudSat. Adding the precipitating ice to the cloud ice increased this to close to 40 – 50%. Close to 500 hPa the model ice water content is often twice as much as CloudSat. In all cases examined, the convective signature contributes the largest portion to the total ice water content.

Changes in ice water content between day and night differ between the model and CloudSat (Fig. 7). There is a large daytime signature in the CPI for the TCL region, and LSPI and cloud ice follow this with a lower magnitude. CloudSat shows the same sign above 300 hPa, but gives higher night time values below. This vertical change in CloudSat day-night difference tends to be a feature unique to the TCL region. In the TWP region (not shown) both model and observation show more ice at night by about $3-5\,\mathrm{mg\,m^{-3}}$.

4.3.3 Sensitivity to fall speed

In the model, ice water content at each level is greatly influenced by the fall speed parametrizations as they are used in calculating sedimentation rate cloud ice and for converting the precipitation fluxes to ice water densities for some of the large-scale and convective precipitating ice microphysical processes. Several fall speeds have been considered when converting the model ice fluxes to ice densities using Eq. 2. They are: (1) a mass-dependent fall speed for the CPI (see Eq. 5.39 in the IFS documentation: `www.ecmwf.int/research/ifsdocs/CY31r1`), (2) a mass-independent fall speed using Eq. 1, and (3) a constant fall speed of $1\,\mathrm{m\,s^{-1}}$ across the entire domain.

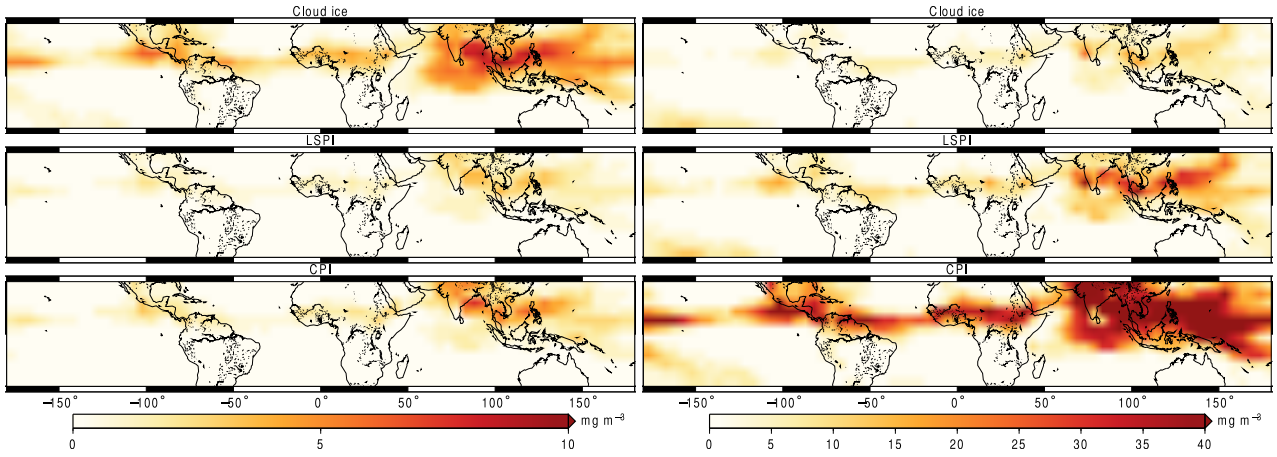

(a) 200 hPa (b) 400 hPa

Fig. 9: Horizontal distribution of ice in EC Earth at 200 hPa and 400 hPa during JJA. Top panel: cloud ice, middle panel: LSPI, and bottom panel: CPI.

The effect of changing the parametrized fall speeds is most notable below 300 hPa (no figures shown). Using the mass-dependent fall speed produces unrealistically high ice water content with values well above 60 mg m^{-3}. Applying the remaining mass-independent fall speeds only results in scaling the ice water content profile without changing the overall shape. This study uses the mass-independent fall speed with a reference speed of 1 m s^{-1} because it produces a reasonable representation of the model's IWC vertical profile.

Table 1: Average difference between EC Earth and Era-Interim for the Tropics for the variables in Fig. 10.

Variable	Difference	Unit
Temperature (T)	-0.5	[K]
Specific humidity (SH)	1.3	[mg kg^{-}1]
RH	3.9	[%]
Cloud fraction (CF)	7.2	[%]
High cloud coverage (HCC)	6.8	[%]
Cloud ice (CI)	0.7	[mg m^{-3}]
Ice water path (IWP)	4.4	[g m^{-2}]
Outgoing longwave radiation (OLR)	-2.0	[W m^{-2}]

4.4 Comparison with ERA-Interim

Figure 10 depicts a two-year, tropical monthly-mean time-series comparison between EC Earth and ERA-Interim. The Era-Interim 12 UTC analyses, the subsequent 24 hour forecast, and the EC Earth state at 12 UTC. With the exception of ice water path, OLR, and high cloud coverage, all other variables represent conditions at 200 hPa. IWP in this section is calculated excluding precipitating ice. The time series covers the period 2006 – 2007. This is a deviation from the rest of the datasets in this study and is motivated by the simple need for a longer time series.

EC Earth takes its initial and surface boundary conditions from ERA-interim, but despite this coupling, significant differences can be seen. The impact of the initial conditions appears to disappear inside a week or less as the differences for the first month do not stand out in any way. In all cases where the difference between EC Earth and ERA-Interim has a constant sign, the 24 hour forecast goes in the direction of EC Earth. This is also expected as similar IFS versions are used. While the shift in the 24 hour forecast can be seen as an indication of the minimum effect assimilation of observations has on the TUTW variables in Era-Interim, assimilation is likely not the only cause to the differences seen in Fig. 10. Changes in model physics are likely involved. In fact, the differences are consistent with what is believed to be the most influential change for this study. This is the modified convection entrainment parametrization, that increases the sensitivity of convection in the model to moisture and, hence, should generate more cloud ice and clouds in the tropical upper troposphere (Bechtold et al, 2008).

Table. 1 shows the average differences for each variable. In EC Earth the temperature is colder by approximately 0.5 K, the RH is higher by 4 pp, the cloud fraction by 7 pp, and the high cloud coverage by ∼7 pp. A clear anti-correlation between T and RH/cloud fraction can be seen in Fig. 10. The EC Earth OLR is on average 2 W m^{-2} lower than ERA-Interim, but the deviation is, for some periods, close to zero. The OLR difference follows largely the pattern for T and RH, but cannot be completely explained by those variables. In summary, IFS (as a model) has a tendency towards a cooler and more cloudy tropical upper atmosphere compared to the constraints given by the data assimilated by ERA-Interim, and this results in a decreased OLR.

4.5 Outgoing longwave radiation

The model's OLRs are sampled to match the CERES SSF observation which is a 24 hour mean based on the two A-Train overpasses. Since the daily mean longwave radiation budget in the Tropics is sensitive to the diurnal cycle of convection, deviations from the true daily mean will occur. It should be noted that CERES OLR$_{CS}$ can include remain-

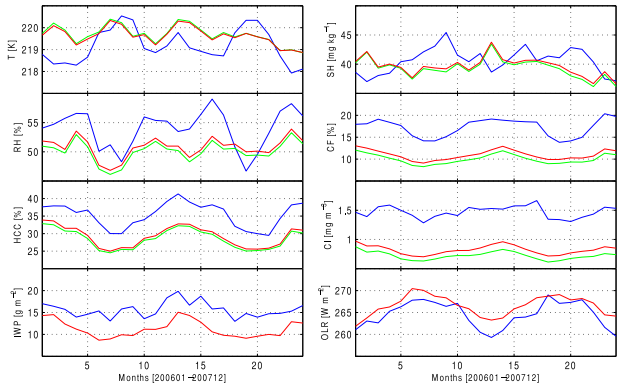

Fig. 10: Time-series of monthly means from 2006 to 2007 in the Tropics at 12 UTC. Temperature (T), specific humidity (SH), RH, cloud fraction, and cloud ice are taken at 200 hPa. High cloud coverage is the total high cloud cover. Ice water path (see text) and OLR are vertically integrated variables. Blue: EC Earth, green: ERA-Interim analyses, and red: Era-Interim 24 hour forecast from the 12 UTC analyses. The ERA-Interim archive does not include OLR and ice water path in the analyses.

Table 2: Seasonal and regional values for OLR (normal font), OLR_{CS} (bold font), and OLR_{CE} (italic font), in $W\,m^{-2}$. Third column from the left: CERES data and far right column: difference between EC Earth and CERES. The uncertainties for CERES OLRs are given in parenthesis.

OLR statistics							
Region	Season	CERES ±(5 7 5)			EC Earth -CERES		
Tropics	DJF	259	**291**	*32*	2	**-7**	*-9*
	MAM	260	**291**	*31*	5	**-5**	*-9*
	JJA	260	**289**	*29*	3	**-4**	*-7*
	SON	258	**290**	*32*	6	**-4**	*-10*
TCL	DJF	231	**282**	*51*	14	**-6**	*-19*
	MAM	232	**281**	*49*	8	**-5**	*-13*
	JJA	242	**282**	*40*	23	**0**	*-23*
	SON	225	**279**	*54*	11	**-4**	*-14*
TWP	DJF	232	**287**	*54*	14	**-2**	*-15*
	MAM	236	**288**	*51*	11	**-4**	*-14*
	JJA	225	**283**	*58*	3	**-6**	*-9*
	SON	225	**285**	*60*	15	**-4**	*-19*
TSW	DJF	272	**293**	*21*	2	**-4**	*-6*
	MAM	282	**297**	*15*	-8	**-6**	*2*
	JJA	286	**298**	*11*	5	**0**	*-4*
	SON	280	**295**	*15*	6	**-1**	*-7*

ing effects of clouds and how it is measured deviates from how the model calculates its OLR_{CS} (Sec. 3.6). The latter aspect makes this not a true "like-with-like" comparison, the assumption here is that the large uncertainty estimate applied should cover for these systematic differences.

4.5.1 Assessment of observations

Table 2 shows seasonal and regional statistics of the mean CERES OLR, OLR_{CS}, and OLR_{CE}. The geographical distribution is shown in Fig. 11 for JJA season. Seasonal changes in the mean outgoing longwave radiation across the Tropics varies about $\sim 2\,W\,m^{-2}$. Regionally, such changes are largest ($17\,W\,m^{-2}$) over the TCL region. For OLR_{CS} seasonal changes are small, $\sim 3\,W\,m^{-2}$, both regionally and for the entire Tropics. Over the Sahara desert, in about 0.3% of the dataset, OLR is frequently greater than OLR_{CS}. To remove such systematic effects, above rounding errors, no data where OLR is more than $2\,W\,m^{-2}$ above the OLR_{CS} are included in the calculation of OLR_{CE}. The effects of clouds on CERES OLR is $\sim 30\,W\,m^{-2}$ across the Tropics but can be as high as $59\,W\,m^{-2}$ in the TWP region.

4.5.2 Comparison between model and observations

Table 2, far right column, shows the difference, CERES-EC Earth. The geographical distribution of these differences is illustrated in Fig. 11. For the Tropics, the annual OLR average is on the positive limit of the CERES uncertainty. While the model agrees fairly well with the general horizontal distribution of CERES OLR, there are major regional differences, exceeding $\pm 20\,W\,m^{-2}$. Similar horizontal distributions are found for other seasons (not shown) as well. Over TCL region there is generally higher OLR in the model but in various smaller areas over water there are equally large negative bias. Desert areas, such as Australia and parts of the Sahara, show a small negative bias. The TSW region is the only region with both positive and negative seasonal means.

OLR_{CS} is generally lower in the model but, throughout, the seasonal means are within the uncertainty of CERES. In Fig. 11 there are some similarities between ΔOLR and ΔOLR_{CS}, except, e.g., over the TWP region where the two differences have opposite sign.

The ΔOLR_{CE} panel illustrates a mainly negative bias in EC Earth and, with the exception of single value, is also what Table 2 shows. Both CERES and EC Earth show the most intense OLR_{CE} in the TWP region but differ in magnitude. The TCL region is the most clear example on systematic underestimation of OLR_{CE}. TWP contains, for JJA, a peculiar region of large positive bias in the middle of negative biases.

5 Discussion and summary

Comparison of climate models with observations is important, both to understand the present performance and to guide their development. Space-based instruments are the only viable data source for assessments on an overall level. However, a comparison between satellite and model data are far from straightforward and to highlight such issues, from a general perspective, is an objective of this study.

A first limitation of satellite measurements is that spatial and temporal coverage are not complete. Some aspects are handled easily, such as to sample the model data at the local time of the satellite overpasses. The availability of satellite data depends, though, on the atmospheric state, for example, the amount of cloud coverage will severely affect AIRS retrieval algorithm or saturate the CALIPSO signal

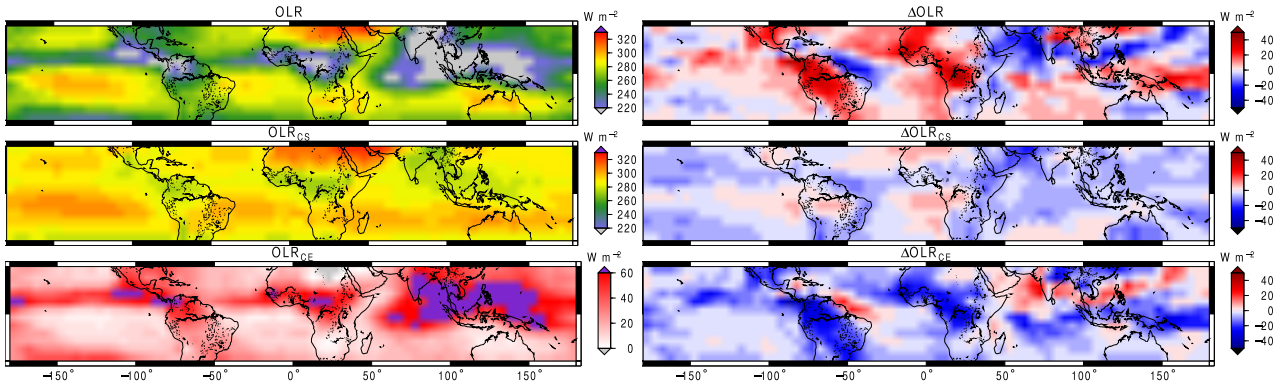

(a) CERES (b) EC Earth - CERES

Fig. 11: (a) CERES. Top panel: OLR, middle panel: OLR_{CS}, bottom panel: OLR_{CE}. (b) Difference (EC Earth -CERES) of OLR. Top panel: OLR, middle panel: OLR_{CS}, bottom panel: OLR_{CE}.

very quickly. When these problems have been overcome, the next step is to judge the significance level of the difference between model and observational data. This question can be surprisingly difficult, as retrieval uncertainties are not reported in a consistent manner. For example, no direct error budget for the CERES OLR data was found. For this study we provide random and systematic error estimates, where possible.

A-train satellites are used here. A first advantage of a satellite constellation is that complementary datasets can be obtained for several variables, decreasing the impact of some problems discussed above. Further, this made it possible to practically incorporate a relatively detailed comparison of four variables, while most earlier studies have considered the variables in isolation. This step forward should help to identify the source to model shortcomings. Some discussion in this direction is found below, but is primarily left for future work.

The comparison with ERA-Interim is not completely consistent with the idea of "seamless prediction", as not exactly the same IFS is used in EC Earth, but helped to illustrate some of the tendencies of the IFS model. The observations assimilated by ERA-Interim give relatively weak constrains for the part of the atmosphere of concern, and the comparison is of lower value for establishing model biases, potentially with the exception for temperature where EC Earth was found to be on the cold side.

EC Earth's RH is mainly consistent with the observations, but the measurements have still large error margins. For example, there is a clear difference between mean RH of EC Earth and ERA-Interim at 200 hPa (Fig. 10), but the satellite sensors cannot provide guidance on evaluating this deviation. The most clear systematic deviations were found in convective active regions (Fig. 2). In these regions EC Earth's day-night differences appear too low around 150 hPa, and EC Earth underestimates RH at 400 – 500 hPa, with a too strong vertical RH gradient above as a result.

The assessment of cloud variables must consider measurement sensitivity and model definitions. EC Earth was estimated to cover clouds somewhat below the detection threshold in CALIPSO (set by the sensor's daytime sensitivity). However, it was judged that this explained only a marginal part of the large difference to cloud fraction around 150 hPa (Fig. 4), and EC Earth was classified as being too "cloudy" above 200 hPa. The combination of Figs. 2 and 10 shows that ERA-Interim has an average cloud fraction similar to the CALIPSO datset at 200 hPa, while EC Earth cloud fraction is up to 100% higher. A clear correlation between the EC Earth-ERA differences in RH and cloud fraction was noted (Sec. 4.4), and as the formation of clouds in EC Earth operates with a RH threshold (Sec. 2.6), it seems likely that the too high cloud fraction above 200 hPa originates, at least partly, by the increased RH.

Below 250 hPa, the situation is reversed. The EC Earth cloud fraction is here much lower than the best observations, even considering the difference in how precipitation is classified as "cloudy" (CloudSat) or not (EC Earth). This is again consistent with findings for RH. In fact, both the RH and cloud fraction profiles in EC Earth have their minima around 400 hPa, again indicating the strong coupling between the two variables in EC Earth. A plausible explanation to these features is that EC Earth underestimates the amount of convection detrainment in this altitude region, around the ITCZ. The fact that EC Earth's RH and cloud fraction at 400 hPa match the observations much better at the most south latitudes in Figs. 3 and 5, i.e., the latitudes furthest away from ITCZ, can be an indication on the mid-level transport of moisture is better handled at extratropical latitudes.

EC Earth, as with most models, makes a distinction between "cloud" and "precipitating" ice, where precipitating ice is treated as a flux and lacking a clearly defined ice mass. While CloudSat's ice water content is an estimate of the complete ice mass, the precipitating ice ice mass is estimated by assuming a fall speed (Eq. 1 with $v_{ref} = 1\,\mathrm{m\,s^{-1}}$). However, EC Earth uses, internally, several, partly inconsistent, fall speeds. Different parameterisations are tested for the conversion (not shown) from flux to ice water content. Though this gives a large uncertainty for EC Earth's ice water content, it does not affect the main conclusions

(Fig. 7): (1) EC Earth underestimates the ice water content above 250 hPa. (2) Precipitating ice generated by convection causes an overestimation of ice water content below 400 hPa.

Chen et al (2011) approached this problem from the other direction. They partitioned the CloudSat ice water content, based on the particle size distribution (PSD) applied in the retrieval and assuming that cloud ice/precipitating ice corresponds to particles below/above some specified size, D_c. Only their results from latitudes inside $\pm 30°$ are discussed here. They consistently find the highest cloud ice between 300 and 200 hPa, but the cloud ice vertical profile is strongly affected by the value of D_c. The study reports data from the IFS version of ERA-Interim, and indicates a good agreement for $D_c = 150\,\mu$m. The higher cloud ice in EC Earth (Sec. 4.4) would require a higher D_c for a similar fit. If the commonly suggested value of $D_c = 100\,\mu$m is applied, both ERA-interim and EC Earth overestimates the cloud ice, particularly at altitudes below 300 hPa. However, these results can only be taken as indicative, as they rely on that the PSD used in the CloudSat retrievals is the best possible.

The tropical average OLR of EC Earth is inside the error margins of the observations (Table 2), but this is achieved by a balance between negative and positive errors (Fig. 11). The two main terms are a low bias in clear-sky OLR and a general underestimation of the impact of clouds on OLR ($\mathrm{OLR_{CE}}$). There are clear regional patterns in the error for $\mathrm{OLR_{CE}}$ but these are likely to originate in part from similar patterns in the "clear-sky bias" of CERES $\mathrm{OLR_{CS}}$ (see Fig. 3 in Sohn et al (2010)).

The tropical average $\mathrm{OLR_{CE}}$ is $9\,\mathrm{W\,m^{-2}}$ lower in EC Earth than for CERES. As pointed out by Waliser et al (2011), the negligence of precipitating ice in the radiation calculations, as done in EC Earth, affects the $\mathrm{OLR_{CE}}$ significantly. However, as Waliser et al (2011) estimated, the maximum regional impact is about $10\,\mathrm{W\,m^{-2}}$, this does not explain the complete underestimation of $\mathrm{OLR_{CE}}$ in EC Earth.

The solution to the underestimation of EC Earth's $\mathrm{OLR_{CE}}$ is not just to increase the tropical average cloud ice, due to the non-linearity between cloud ice water path and emissivity (Eqs. 5 and 6). That is, neither average ice water content, cloud fraction, nor the product between the two variables, are linearly proportional to average $\mathrm{OLR_{CE}}$. For example, the areas where EC Earth overestimates $\mathrm{OLR_{CE}}$ (Fig. 11), do not stand out particularly in the fields of cloud ice (Fig. 9). Accordingly, any attempts to improve the $\mathrm{OLR_{CE}}$ in EC Earth should consider the ice water content probability distribution function, not just the average cloud fraction and ice water content, as is done here.

The comparison with ERA-Interim is worth considering also in this context. The OLR is found to be $2\,\mathrm{W\,m^{-2}}$ lower in EC Earth (Table 1). Already the lower temperature explains a part of the decrease in OLR. For tropical clear-sky conditions and a constant absolute humidity, a 0.5 K colder troposphere decreases the OLR with about $0.7\,\mathrm{W\,m^{-2}}$ (Buehler et al, 2006, Fig. 6). The average tropical $\mathrm{OLR_{CE}}$ in EC Earth is $22\,\mathrm{W\,m^{-2}}$. That is, the EC Earth $\mathrm{OLR_{CE}}$ seems to deviate from ERA-Interim with less than 10%, which is a surprisingly low number considering the increases of about 20%, 70% and 100% for high cloud coverage, cloud fraction and cloud ice, respectively. The reason for this behaviour is not investigated, such as, if the extra cloudiness in EC Earth occurs primarily at very low and high ice water content, but this apparent "robustness" in $\mathrm{OLR_{CE}}$ is important to understand before confident cloud feedback estimates can be provided.

Acknowledgements The authors would like to thank Klaus Wyser (SMHI), Simona Ştefănescu (ECMWF) for their aid in setting up and running the model. Special thanks to George E. Ferriter for his linguistic critique of the article. The CERES data are obtained from the NASA Langley Research Centre EOSDIS Distributed Archive Center. Discussions with Norman Loeb and Dave Doelling were beneficial. We would like to thank the following organisations for their open access to the data used in this study: GSFC Earth Science Data and Information Services Center (GES DISC), the Jet Propulsion Laboratory, CloudSat Data Processing Center, and ISCCP, and IPSL/LMD for CALIPSO-GOCCP dataset available at `http://climserv.ipsl.polytechnique.fr/cfmip-obs`

References

Austin RT, Heymsfield AJ, Stephens GL (2009) Retrieval of ice cloud microphysical parameters using the CloudSat millimeter-wave radar and temperature. J Geophys Res 114(D8):D00A23, DOI 10.1029/2008JD010049

Bechtold P, Köhler M, Jung T, Doblas-Reyes F, Leutbecher M, Rodwell MJ, Vitart F, Balsamo G (2008) Advances in simulating atmospheric variability with the ECMWF model: From synoptic to decadal time-scales. Q J R Meteorol Soc 134(634):1337–1351, DOI 10.1002/qj.289

Buehler SA, von Engeln A, Brocard E, John VO, Kuhn T, Eriksson P (2006) Recent developments in the line-by-line modeling of outgoing longwave radiation. J Quant Spectrosc Radiat Transfer 98(3):446–457, DOI 10.1016/j.jqsrt.2005.11.001

Chen WT, Woods CP, Li JLF, Waliser DE, Chern JD, Tao WK, Jiang JH, Tompkins AM (2011) Partitioning cloudsat ice water content for comparison with upper-tropospheric ice in global atmospheric models. J Geophys Res DOI 10.1029/2010JD015179

Chepfer H, Bony S, Winker D, Chiriaco M, Dufresne J, Sèze G (2008) Use of CALIPSO lidar observations to evaluate the cloudiness simulated by a climate model. Geophys Res Lett 35(15):L15,704, DOI 10.1029/2008GL034207

Chepfer H, Bony S, Winker D, Cesana G, Dufresne JL, Minnis P, Stubenrauch CJ, Zeng S (2010) The GCM Oriented Calipso Cloud Product CALIPSO-GOCCP. J Geophys Res 115:D00H16, DOI 10.1029/2009JD012251

Dee DP, Uppala SM, Simmons AJ, Berrisford P, Poli P, Kobayashi S, Andrae U, Balmaseda MA, Balsamo G, Bauer P, Bechtold P, Beljaars ACM, van de Berg L, Bidlot J, Bormann N, Delsol C, Dragani R, Fuentes M, Geer AJ, Haimberger L, Healy SB, Hersbach H, Hólm

EV, Isaksen L, Kållberg P, Köhler M, Matricardi M, McNally AP, Monge-Sanz BM, Morcrette JJ, Park BK, Peubey C, de Rosnay P, Tavolato C, Thépaut JN, Vitart F (2011) The ERA-Interim reanalysis: configuration and performance of the data assimilation system. Q J R Meteorol Soc 137(656):553–597, DOI 10.1002/qj.828

Delanoë J, Hogan RJ (2010) Combined CloudSat-CALIPSO-MODIS retrievals of the properties of ice clouds. J Geophys Res 115(D00H29), DOI 10.1029/2009JD012346

Ebert EE, Curry JA (1992) A parameterization of ice cloud optical properties for climate models. J Geophys Res 97(D4):3831–3836, DOI 10.1029/91JD02472

Ekström M, Eriksson P, Read WG, Milz M, Murtagh DP (2008) Comparison of satellite limb-sounding humidity climatologies of the uppermost tropical troposphere. Atmos Chem Phys 8(2):309–320, DOI 10.5194/acp-8-309-2008

Eliasson S, Buehler SA, Milz M, Eriksson P, John VO (2011) Assessing observed and modelled spatial distributions of ice water path using satellite data. Atmos Chem Phys 11(1):375–391, DOI 10.5194/acp-11-375-2011

Eriksson P, Ekström M, Rydberg B, Wu DL, Austin RT, Murtagh DP (2008) Comparison between early Odin-SMR, Aura MLS and CloudSat retrievals of cloud ice mass in the upper tropical troposphere. Atmos Chem Phys 8(7):1937–1948, DOI 10.5194/acp-8-1937-2008

Eriksson P, Rydberg B, Johnston M, Murtagh DP, Struthers H, Ferrachat S, Lohmann U (2010) Diurnal variations of humidity and ice water content in the tropical upper troposphere. Atmos Chem Phys 10:11,519–11,533, DOI 10.5194/acp-10-11519-2010

Evan AT, Heidinger AK, Vimont DJ (2007) Arguments against a physical long-term trend in global ISCCP cloud amounts. Geophys Res Lett 34(4):L04,701, DOI 10.1029/2006GL028083

Folkins I, Kelly KK, Weinstock EM (2002) A simple explanation for the increase in relative humidity between 11 and 14 km in the tropics. J Geophys Res 107(D23):4736, DOI 10.1029/2002JD002185

Geleyn J, Hollingsworth A (1979) An economical analytical method for the computation of the interaction between scattering and line absorption of radiation. Beitr Phys Atm 52:1–16

Gettelman A, Collins WD, Fetzer EJ, Eldering A, Irion FW, Duffy PB, Bala G (2006) Climatology of upper-tropospheric relative humidity from the Atmospheric Infrared Sounder and implications for climate. J Clim 19(23):6104–6121, DOI 10.1175/JCLI3956.1

Hazeleger W, Severijns C, Semmler T, Stefãnescu S, Yang S, Wang X, Wyser K, Dutra E, Baldasano JM, Bintanja R, et al (2010) EC-Earth: A seamless earth system prediction approach in action. Bull Amer Met Soc 91(10):1357–1363, DOI 10.1175/2010BAMS2877.1

Hazeleger W, Wang X, Severijns C, Stefãnescu S, Bintanja R, Sterl A, Wyser K, Semmler T, Yang S, van den Hurk B, van Noije T, van der Linden E, van der Wiel K (2011) EC-Earth V2.2: description and validation of a new seamless earth system prediction model. Clim Dyn pp 1–19, DOI 10.1007/s00382-011-1228-5

Heymsfield AJ, Iaquinta J (2000) Cirrus crystal terminal velocities. J Atmos Sci 57(7):916–938, DOI 10.1175/1520-0469(2000)057⟨0916:CCTV⟩2.0.CO;2

Heymsfield AJ, Matrosov S, Baum B (2003) Ice water path-optical depth relationships for cirrus and deep stratiform ice cloud layers. J Appl Meteorol 42(10):1369–1390, DOI 10.1175/1520-0450(2003)042⟨1369:IWPDRF⟩2.0.CO;2

Kärcher B, Lohmann U (2002) A parameterization of cirrus cloud formation: homogeneous freezing including effects of aerosol size. J Geophys Res 107(D23):4698, DOI 10.1029/2001JD001429

Kessler E (1969) On the distribution and continuity of water substance in atmospheric circulations. Meteorol Monogr 10(32):84

Liang C, Eldering A, Gettelman A, Tian B, Wong S, Fetzer E, Liou K (2011) Record of tropical interannual variability of temperature and water vapor from a combined AIRS-MLS data set. J Geophys Res 116:D06,103, DOI 10.1029/2010JD014841

Liu C, Zipser EJ (2009) Implications of the day versus night differences of water vapor, carbon monoxide, and thin cloud observations near the tropical tropopause. J Geophys Res 114(D9):D09,303, DOI 10.1029/2008JD011524

Liu C, Zipser EJ, Mace GG, Benson S (2008) Implications of the differences between daytime and nighttime cloudsat observations over the tropics. J Geophys Res 113(D8):D00A04, DOI 10.1029/2008JD009783

Liu JY, Orville HD (1969) Numerical modeling of precipitation and cloud shadow effects on mountain-induced cumuli. J Atmos Sci 26(6):1283–1298, DOI 10.1175/1520-0469(1969)026⟨1283:NMOPAC⟩2.0.CO;2

Loeb NG, Kato S (2002) Top-of-atmosphere direct radiative effect of aerosols over the tropical oceans from the Clouds and the Earth's Radiant Energy System CERES satellite instrument. J Clim 15(12):1474–1484, DOI 10.1175/1520-0442(2002)015⟨1474:TOADRE⟩2.0.CO;2

Loeb NG, Wielicki BA, Doelling DR, Smith GL, Keyes DF, Kato S, Manalo-Smith N, Wong T (2009) Toward optimal closure of the Earth's top-of-atmosphere radiation budget. J Clim 22(3):748–766, DOI 10.1175/2008JCLI2637.1

Maddy ES, Barnet CD (2008) Vertical resolution estimates in Version 5 of AIRS operational retrievals. IEEE Trans Geosci Remote Sensing 46(8):2375–2384, DOI 10.1109/TGRS.2008.917498

Meehl GA, Stocker TF, Collins WD, Friedlingstein P, Gaye AT, Gregory JM, Kitoh A, Knutti R, Murphy JM, Noda A, Raper SCB, Watterson IG, Weaver AJ, Zhao ZC (2007) Cilmate models and their evaluation. In: Climate change 2007: The Physical Science Basis. Contribution of Working Group I to the Fourth Assessment Report of the Intergovernmental Panel on Climate Change [Solomon, S. and Qin, D. Manning, M. and Chen, Z.

and Marquis, M. and Averyt, K. B. and Tignor, M. and Miller, H. L. (eds.)]. Cambridge University Press, Cambridge, United Kingdom and New York, NY, USA.

Mlawer EJ, Taubman SJ, Brown PD, Iacono MJ, Clough SA (1997) Radiative transfer for inhomogeneous atmospheres: RRTM, a validated correlated-k model for the longwave. J Geophys Res 102(D14):16,663–16,682, DOI 10.1029/97JD00237

Murphy DM, Koop T (2005) Review of the vapour pressures of ice and supercooled water for atmospheric applications. Q J R Meteorol Soc 131(608):1539–1565, DOI 10.1256/qj.04.94

Nazaryan H, McCormick MP, Menzel WP (2008) Global characterization of cirrus clouds using CALIPSO data. J Geophys Res 113(D16):D16,211, DOI 10.1029/2007JD009481

Palmer TN, Doblas-Reyes FJ, Weisheimer A, Rodwell MJ (2009) Toward Seamless Prediction: Calibration of Climate Change Projections Using Seasonal Forecasts Reply. Bull Amer Met Soc 90(10):1551–1554, DOI 10.1175/2009BAMS2916.1

Protat A, Delanoë J, O'Connor EJ, L'Ecuyer TS (2010) The evaluation of CloudSat and CALIPSO ice microphysical products using ground-based cloud radar and lidar observations. J Atmos Ocean Technol 27(5):793–810, DOI 10.1175/2009JTECHA1397.1

Räisänen P (1998) Effective longwave cloud fraction and maximum-random overlap of clouds: a problem and a solution. MWR 126(12):3336–3340, DOI 10.1175/1520-0493(1998)126⟨3336:ELCFAM⟩2.0.CO;2

Read WG, Lambert A, Bacmeister J, Cofield RE, Christensen LE, Cuddy DT, Daffer WH, Drouin BJ, Fetzer E, Froidevaux L, Fuller R, Herman R, Jarnot RF, Jiang JH, Jiang YB, Kelly K, Knosp BW, Kovalenko LJ, Livesey NJ, Liu HC, Manney GL, Pickett HM, Pumphrey HC, Rosenlof KH, Sabounchi X, Santee ML, Schwartz MJ, Snyder WV, Stek PC, Su H, Takacs LL, Thurstans RP, Vömel H, Wagner PA, Waters JW, Webster CR, Weinstock EM, Wu DL (2007) Aura Microwave Limb Sounder upper tropospheric and lower stratospheric H_2O and relative humidity with respect to ice validation. J Geophys Res 112:D24S35, DOI 10.1029/2007JD008752

Rossow WB, Garder L (1984) Selection of map grid for data analysis and archival. J Clim Appl Meteorol 23(8):1253–1257, DOI 10.1175/1520-0450(1984)023⟨1253:SOAMGF⟩2.0.CO;2

Rossow WB, Schiffer RA (1991) ISCCP cloud data products. Bull Amer Met Soc 72(1):2–20, DOI 10.1175/1520-0477(1991)072⟨0002:ICDP⟩2.0.CO;2

Rossow WB, Schiffer RA (1999) Advances in understanding clouds From ISCCP. Bull Amer Met Soc 80(11):2261–2287, DOI 10.1175/1520-0477(1999)080⟨2261:AIUCFI⟩2.0.CO;2

Soden BJ (2000) The diurnal cycle of convection, clouds, and water vapor in the tropical upper troposphere. Geophys Res Lett 27(15):2173–2176, DOI 10.1029/2000GL011436

Sohn BJ, Nakajima T, Satoh M, Jang HS (2010) Impact of different definitions of clear-sky flux on the determination of longwave cloud radiative forcing: Nicam simulation results. Atmos Chem Phys 10(23):11,641–11,646, DOI 10.5194/acp-10-11641-2010

Stephens GL, Vane DG, Boain RJ, Mace GG, Sassen K, Wang Z, Illingworth AJ, O'connor EJ, Rossow WB, Durden SL, et al (2002) The CloudSat Science Team, 2002: The CloudSat mission and the A-train. Bull Amer Met Soc 83(12):1771–1790, DOI 10.1175/BAMS-83-12-1771

Sun W, Videen G, Kato S, Lin B, Lukashin C, Hu Y (2011) A study of subvisual clouds and their radiation effect with a synergy of CERES, MODIS, CALIPSO, and AIRS data. J Geophys Res 116(D22):D22,207, DOI 10.1029/2011JD016422

Tian B, Soden BJ, Wu X (2004) Diurnal cycle of convection, clouds, and water vapor in the tropical upper troposphere: Satellites versus a general circulation model. J Geophys Res 109(D16):D10,101, DOI 10.1029/2003JD004117

Tiedtke M (1993) Representation of clouds in large-scale models. Mon Wea Rev 121(11):3040–3061, DOI 10.1175/1520-0493(1993)121⟨3040:ROCILS⟩2.0.CO;2

Tompkins AM, Gierens K, Rädel G (2007) Ice supersaturation in the ECMWF integrated forecast system. Q J R Meteorol Soc 133:53–63, DOI 10.1002/qj.14

Waliser DE, Li JLF, Woods CP, Austin RT, Bacmeister J, Chern J, Genio AD, Jiang JH, Kuang Z, Meng H, Minnis P, Platnick S, Rossow WB, Stephens GL, Sun-Mack S, Tao WK, Tompkins AM, Vane DG, Walker C, Wu D (2009) Cloud ice: a climate model challenge with signs and expectations of progress. J Geophys Res 114:D00A21, DOI 10.1029/2008JD010015

Waliser DE, Li JLF, L'Ecuyer TS, Chen WT (2011) The impact of precipitating ice and snow on the radiation balance in global climate models. Geophys Res Lett 38(6):L06,802, DOI 10.1029/2010GL046478

Wang PH, Minnis P, McCormick MP, Kent GS, Skeens KM (1996) A 6-year climatology of cloud occurrence frequency from Stratospheric Aerosol and Gas Experiment II observations (1985-1990). J Geophys Res 101(D23):29,407–29,429, DOI 10.1029/96JD01780

Waters JW, Froidevaux L, Harwood RS, Jarnot RF, Pickett HM, Read W, Siegel PH, Cofield RE, Filipiak MJ, Flower DA, Holden JR, Lau GK, Livesey NJ, Manney GL, Pumphrey HC, Santee ML, Wu WL, Cuddy DT, Lay RR, Loo MS, Perun VS, Schwartz MJ, Stek P, Thurstans RP, Boyles MA, Chandra KM, Chavez MC, Chen GS, Chudasama BV, Dodge R, Fuller RA, Girard MA, Jiang JH, Jiang YB, Knosp BW, LaBelle R, Lam JC, Lee KA, Miller D, Oswald JE, Patel NC, Pukala DM, Quintero O, Scaff DM, Snyder WV, Tope MC, Wagner P, Walch M (2006) The Earth Observing System Microwave Limb Sounder (EOS MLS) on the Aura satellite. IEEE Trans Geosci Remote Sensing 44(5):1075–1092, DOI 10.1109/TGRS.2006.873771

Wielicki BA, Barkstrom BR, Harrison EF, Lee RB, Smith GL, Cooper JE (1996) Clouds and the Earth's Radiant Energy System CERES: An earth observing system experiment. Bull Amer Met Soc 77(5):853–868, DOI 10.1175/1520-0477(1996)077⟨0853:CATERE⟩2.0.CO;2

Winker DM, Hunt WH, McGill MJ (2007) Initial performance assessment of CALIOP. Geophys Res Lett 34(19):L19,803, DOI 10.1029/2007GL030135

Wu DL, Austin RT, Deng M, Durden SL, Heymsfield AJ, Jiang JH, Lambert A, Li JL, Livesey NJ, McFarquhar GM, et al (2009) Comparisons of global cloud ice from MLS, CloudSat, and correlative data sets. J Geophys Res 114:0148–0227, DOI 10.1029/2008JD009946

Yang GY, Slingo J (2001) The diurnal cycle in the tropics. Mon Wea Rev 129:784–801, DOI 10.1175/1520-0493(2001)129⟨0784:TDCITT⟩2.0.CO;2